myjournal manuscript No.
(will be inserted by the editor)

Modeling Arbitrarily Oriented and Reorienting Multiscale Cracks in Composite Materials with Adaptive Multiscale Discrete Damage Theory

Zimu Su, Caglar Oskay*

Department of Civil and Environmental Engineering, Vanderbilt University, Nashville, TN, USA, 37235

Received: date / Revised version: date

Abstract An adaptive multiscale modeling approach based on the multiscale discrete damage theory (MDDT) is established to describe formation of arbitrarily oriented and progressively reorienting cracks at multiple scales in heterogenous materials. MDDT tracks the fracture process over a set of discrete cohesive failure surfaces in the microstructure and consistently bridges the microscopic cracks to the continuum representation of damage at macroscale based on the reduced-order homogenization method. In this manuscript, the adaptation to arbitrary orientation of a crack is achieved using the idea of effective rotation of microstructure which reorients the prescribed failure path at the direction of crack propagation. The MDDT model representing the microstructure is analytically transformed given a crack nucleation orientation and an identification criterion. The performance of the proposed model is demonstrated at the microscale under multiaxial loading conditions. The predictive capabilities of the model are validated using four-point bending test of concrete beam and delamination migration experiments of fiber-reinforced composite cross-ply laminates. The qualitative and quantitative evaluations of crack propagation and reorientation show good agreement with the experimental results.

Send offprint requests to:
* *Corresponding author address:* VU Station B 351831, 2301 Vanderbilt Place, Nashville, TN, USA, 37235. Email: caglar.oskay@vanderbilt.edu

Keywords: Multiscale modeling; Reduced order modeling; Adaptivity; Crack orientation; Heterogeneous material; Delamination migration.

1 Introduction

Composite materials have been widely deployed in aerospace, automotive, civil infrastructure and many other industries due to their high specific strength and stiffness, high damage tolerance and durability. A wide range of sophisticated progressive damage analysis (PDA) approaches that rely on fracture mechanics, continuum damage mechanics, failure criteria and multiscale principles have been developed (see e.g. [1–4]) to predict the failure behavoir of composite materials. Complex features such as branching, merging and kinking are often observed in structural components with complex geometry [5, 6] or under multiaxial/time varying load conditions [7], yet accurate prediction of failure in the presence of such complications using PDA methods remain to be fully addressed.

PDA approaches that leverage multiscale principles offer a new paradigm for modeling complex failure processes in heterogenous materials. In the context of a two scale representation, multiscale PDA methods track failure concurrently at the microscopic scale that resolve material inclusions and matrix, and at the macroscopic

scale over the structural component. Methods that rely on fracture (i.e., discrete) representation of failure at both scales [8, 9], damage (i.e., continuum) representation at both scales [10, 11], and hybrid (discrete-contiuum [12, 13] and continuum-discrete [14] at micro- and macroscales, respectively) have been previously proposed. While most approaches incorporate microstructural processes directly into the structural simulation, they suffer from high computational cost, which limits their applicability. Reduced order modeling to approximate the microstructural response using a coarse basis [4, 15] has been shown to bring down the cost, enough to facilitate large scale analysis (see e.g. [10, 16, 17]). More recently, the authors proposed a reduced-order, discrete-continuum multiscale approach, Multiscale Discrete Damage Theory (MDDT) to study failure in composite materials [12, 13]. MDDT approach tracks failure events in the microstructure along a set of predefined cohesive surfaces. Accumulation of discrete microscopic cracks along these surfaces leads to diffuse damage patterns at the macroscale. MDDT is also endowed with a regularization scheme to alleviate spurious mesh localization effect that may occur due to the continuum description of damage at the macroscale.

In this manuscript, we propose an efficient, MDDT-based multiscale strategy to model crack kinking in composite materials. The primary idea is to adaptively select the coarse basis approximation of failure at the microscale (i.e., as opposed to predefining the cohesive surfaces), and leverage rotational invariances in the microstructure to very efficiently calculate the reduced-order model during the multiscale analysis. The performance as well as the restrictions of the model are assessed in the context of numerical microscale specimens subjected to multi-axial loading by comparing model predictions to direct numerical simulations. The proposed approach is then employed to model re-oriented crack propagation in notched concrete beams under four point bending, and delamination migration in fiber- reinforced cross-ply composite laminates. These two cases have been experimentally investigated in Ref. [18, 19].

The remainder of this manuscript is organized as follows: Section 2 provides a brief overview of MDDT, introduces the concept of and methodology for effective microstructure rotation and the evaluation methodology for microcrack nucleation. Section 3 presents the verification of the proposed model in the context of unnotched specimens, and analysis of crack orientation under multiaxial loading conditions. Sections 4 and 5 respectively include the application of the adaptive MDDT model to four point bending analysis of notched concrete beam and delamination migration modeling with experimental validation. Section 6 provides the conclusions.

2 Adaptive MDDT model

The proposed model is based on and generalizes the Multiscale Discrete Damage Theory (MDDT). This section begins with a brief description of MDDT and the resulting system of reduced order multiscale governing equations. Detailed derivation of the MDDT approach is provided in [12] and omitted herein for brevity.

In the MDDT model, the response at the length scale of microstructure is coupled to the macroscopic scale based on the computational homogenization theory [20, 21]. As shown in Fig. 1, the failure process is modeled by considering cohesive behavior within a set of pre-defined, discrete "potential failure paths" embedded in the microstructure [13, 22]. The microscopic fracture events along one or multiple failure paths are consistently bridged to continuum representation of damage at the macroscale using homogenization principles. The reduced-order approximation is employed to alleviate the high computational cost of evaluating nested multiple non-linear problems defined at micro and macroscopic length scales. An important caveat is that the morphologies and number of failure paths need to be defined a-priori. For a given microstructure geometry and a set of potential failure paths, the microstructural equilibrium is approximated using a reduced order model as a function of a series of influence functions (i.e., numerical Green's functions) and coefficient tensors. These quantities are computed prior to a multiscale simulation, through linear-elastic analyses performed over the microstructure.

Consider a composite material, with its domain denoted as Ω. The macroscopic equilibrium is expressed as:

$$\nabla \cdot \bar{\boldsymbol{\sigma}}\left(\mathbf{x}, t\right) = \mathbf{0}; \quad \mathbf{x} \in \Omega \tag{1}$$

where $\bar{\boldsymbol{\sigma}}$ is the homogenized (i.e., macroscopic) stress. Each macroscopic position $\mathbf{x}$ is associated with a mi-

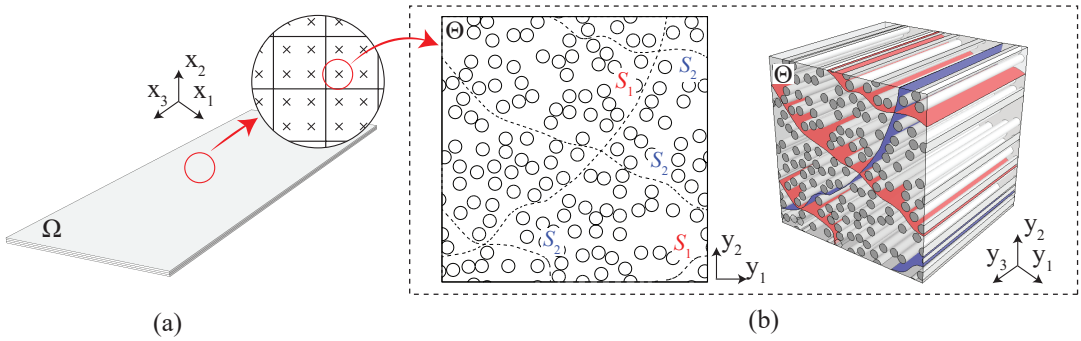

Fig. 1: Multiscale modeling strategy for the composite material using MDDT: (a) macroscopic domain. (b) microstructure domain with multiple failure paths S_1 and S_2.

crostructure domain Θ that includes m failure paths within which progressive evolution of microscale fracture process is tracked. Using the MDDT formulation, the microstructural equilibrium is expressed as the relationship between the homogenized strain $\bar{\boldsymbol{\epsilon}}$ and the cohesive state variables:

$$\mathbf{t}^{(\alpha)}(\mathbf{x},t) - \mathbf{C}^{(\alpha)} : \bar{\boldsymbol{\epsilon}}(\mathbf{x},t) + \sum_{\beta=1}^{m} \mathbf{D}^{(\alpha\beta)} \cdot \boldsymbol{\delta}^{(\beta)}(\mathbf{x},t) = \mathbf{0} \quad (2)$$

where $\boldsymbol{\delta}^{(\alpha)}$ and $\mathbf{t}^{(\alpha)}$ respectively denote the separation vector (i.e., displacement jump) and traction vector that are spatially averaged over the failure path, S_α, $\alpha = 1, 2 \ldots m$. $(\cdot)$ and $(:)$ respectively denote inner and double inner product operators. $\mathbf{C}^{(\alpha)}$, $\mathbf{D}^{(\alpha\beta)}$ are respectively third-order and second order coefficient tensors, which are computed by integrating the influence functions over the microstructure domain and failure paths. They are computed based on linear elastic computations defined over the microstructure domain prior to multiscale analysis, and therefore can be viewed as constitutive parameters that embed microstructural morphology information to the reduced order model. The spatial variation of crack opening displacement and traction along a given failure path are expressed as a function of reduced order basis functions. $\boldsymbol{\delta}^{(\alpha)}$ and $\mathbf{t}^{(\alpha)}$ are the unknown multipliers of the basis functions that fully define spatial variation of crack opening displacement and traction state. It is possible to use different forms of basis functions. In this study, we use piecewise consttant functions, following Ref. [12, 13].

The macroscopic stress $\bar{\boldsymbol{\sigma}}(\mathbf{x},t)$ is expressed as:

$$\bar{\boldsymbol{\sigma}}(\mathbf{x},t) = \bar{\mathbf{L}} : \bar{\boldsymbol{\epsilon}}(\mathbf{x},t) + \sum_{\alpha=1}^{m} \mathbf{Z}^{(\alpha)} \cdot \boldsymbol{\delta}^{(\alpha)}(\mathbf{x},t) \quad (3)$$

where $\bar{\mathbf{L}}$ is the tensor of homogenized elastic moduli, $\mathbf{Z}^{(\alpha)}$ is a third order coefficient tensor that determines the stress contribution due to the separations on the failure path, S_α. The governing equations of the reduced order multiscale system is closed by introducing the macroscopic boundary conditions and a cohesive law that describes the traction-separation relationship along the failure paths. The traction-separation relationship relates the spatially averaged traction and separation fields. We further note that unlike reduced order methods such as non-uniform transformation field analysis [23] which require nonlinear response of the microstructure to build the reduced order model, MDDT only uses the elastic properties of the constituents, the morphology of the microstructure and the failure paths. The form of the traction-separation relationship (e.g., bilinear, exponential, etc.) does not alter the reduced order formulations (i.e. Eq. 1 and 2) and any form can be used to close to the reduced order model.

In the current formulation, the macroscopic constitutive response deviates from linearity due to the onset of fracture process within one or multiple failure paths (i.e. $\boldsymbol{\delta}^{(\alpha)} > 0$ for any subset of $\{1, 2 \ldots, m\}$). The behavior of the matrix and the fiber is otherwise considered elastic. While it is possible to consider additional nonlinear processes (e.g., shear nonlinearity within the matrix), inclusion of these effects is beyond the scope of the current study, and requires extension of the MDDT for-

mulation to incorporate phase eigenstrains as described in Ref. [24].

2.1 Cohesive model

The general MDDT formulation admits any form of cohesive constitutive laws and the cohesive law operates on the failure-path averaged tractions and separations. This work adopts the classical bilinear law [25], wherein the traction-separation relationship is expressed as:

$$\mathbf{t}^{(\alpha)} = (1-\omega^{(\alpha)})\mathbf{K}^{(\alpha)} \cdot \boldsymbol{\delta}^{(\alpha)} \tag{4}$$

where $\mathbf{K}^{(\alpha)}$ is cohesive stiffness. While the proposed formulation admits anistropic cohesive stiffness, we assume the stiffness to be isotropic in this study (see e.g., [25–27]): $\mathbf{K}^{(\alpha)} = K^{(\alpha)}\mathbf{I}$, and $\mathbf{I}$ is the second order identity tensor. $\omega^{(\alpha)} \in [0,1]$ is the scalar damage variable. $\omega^{(\alpha)} = 0$ and $\omega^{(\alpha)} = 1$ respectively denote the state of no damage and a cohesionless crack along the failure path. The index for failure path is omitted for brevity in the equations below for simplicity. The expression of the damage variable is:

$$\omega(\kappa) = \begin{cases} 0 & \kappa \leq \nu_c \\ \dfrac{\nu_u\left(\kappa-\nu_c\right)}{\kappa\left(\nu_u-\nu_c\right)} & \nu_c < \kappa \leq \nu_u \\ 1 & \kappa > \nu_u \end{cases} \tag{5}$$

where $\kappa(t) = \max_{\tau\in[0,t]}\{\nu(\tau)\}$ is the history variable of the equivalent separation, $\nu = \sqrt{\delta_N^2+\delta_{S1}^2+\delta_{S2}^2}$. δ_N, δ_{S1} and δ_{S2} are respectively normal and two tangential components of the separation vector. The normal separation is constrained to be positive δ_N ($\delta_N \geq 0$) to avoid interpenetration using a high penalty stiffness in compression loading. ν_c and ν_u in Eq. 5 are respectively the equivalent separation at crack nucleation (i.e. softening onset) and ultimate failure. ν_c is computed based on the following quadratic-form failure initiation criterion [25]:

$$g = \left(\frac{\langle t_N\rangle}{t_{u_{\mathrm{I}}}}\right)^2 + \left(\frac{t_{S1}}{t_{u_{\mathrm{II}}}}\right)^2 + \left(\frac{t_{S2}}{t_{u_{\mathrm{II}}}}\right)^2 - 1 = 0 \tag{6}$$

where t_N, t_{S1} and t_{S2} are respectively normal and two tangential components of the traction vector. $t_{u_{\mathrm{I}}}$ and $t_{u_{\mathrm{II}}}$ are peak strengths at crack nucleation under pure mode-I and mode-II conditions. $\langle\cdot\rangle$ stands for Macaulay brackets to avoid the contribution of negative normal traction to failure criterion. Let the onset separations at peak strength $\delta_{c_{\mathrm{I}}}$, $\delta_{c_{\mathrm{II}}}$ satisfy $t_{u_{\mathrm{I}}} = K\delta_{c_{\mathrm{I}}}$, $t_{u_{\mathrm{II}}} = K\delta_{c_{\mathrm{II}}}$, then ν_c (i.e. the equivalent separation at $g=0$) is given as:

$$\nu_c = \delta_{c_{\mathrm{I}}}\delta_{c_{\mathrm{II}}}\sqrt{\frac{1+{\beta_m}^2}{(\delta_{c_{\mathrm{II}}})^2+(\beta_m\delta_{c_{\mathrm{I}}})^2}} \tag{7}$$

where β_m stands for ratio between the tangential and normal components of separation: $\beta_m = \sqrt{\delta_{S1}^2+\delta_{S2}^2}/\delta_N$.

Ultimate separation ν_u is defined using the B-K criterion [28]:

$$\nu_u = \frac{2}{K\nu_c}\left[G_{\mathrm{I}c} + (G_{\mathrm{II}c}-G_{\mathrm{I}c})\left(\frac{{\beta_m}^2}{1+{\beta_m}^2}\right)^{\eta_{\mathrm{BK}}}\right] \tag{8}$$

where $G_{\mathrm{I}c}$ and $G_{\mathrm{II}c}$ are respectively the mode-I and mode-II critical fracture energies.

Evaluation of Eqs. 1 to 8 describes the full macroscopic response of a composite that undergoes fracture processes emanating from the material microstructure. This reduced representation approximates the microstructural response using a nonlinear system of equations with $3m$ cardinal unknowns (i.e., spatially averaged separation vectors). The size of the basis is therefore defined by the number of failure paths placed in the microstructure. A key aspect of MDDT is that it is also endowed with a regularization methodology, which alleviates mesh-size sensitivity in the macroscopic failure analysis. The mesh size sensitivity is due to the spurious localization of damage that results in element size dependent fracture energy within the failure localization band. The regularization scheme achieves the energetic consistency by adjusting the size of microstructure domain in an effective manner by applying a scaling transformation to the coefficient tensors in the reduced-order model as a function of the macroscopic element size. Govindjee's expression [29] is adopted to determine the characteristic macroscopic element length which is characterized along the normal direction of a failure path.

As further explained in Ref. [12], the crack regularization approach in MDDT bears resemblance to the crack band model (CBM), in that damage at the macroscopic scale is allowed to localize, and the energy dissipated at the element level is adjusted based on the macroscopic element size (albeit in CBM this is achieved in a different way, by adjusting the damage evolution parameters) to achieve energy consistency. It is therefore reasonable

to consider that the structural size effect that can be captured using CBM [30] can also be captured using MDDT. Structural size effect is not investigated in the current study.

2.2 Strategies for selection of failure paths

The idea of predefining and embedding failure paths with fixed orientations in the microstructure was shown to be effective for modeling failure mechanisms, where the crack directions are known a-priori such as splitting crack or transverse matrix cracking in laminated composites structures [12, 13]. The orientations of such cracks are dictated by the direction of the lamination. However, such a strategy is not ideal for modeling cracks, for which the propagation direction is determined by the local stress state and the relative microstructure configuration. A straightforward approach is to pre-define a large number of potential failure paths with different orientations to cover possible cracking scenarios. The direction of crack propagation then naturally arises during the multiscale analysis as the direction of the failure path that fails first from among the finite choices of failure path orientations. This approach requires a high number of failure paths to be deployed to capture the failure behavior accurately (i.e., $m \gg 1$). Since the resulting nonlinear system is dense, the computational cost of evaluating it is $O\left(m^3\right)$ [31], reducing the potential benefits of model order reduction. Another possible approach is to dynamically construct reduced order models on the fly during the multiscale analysis, where a failure path is embedded in the microstructure model when a failure criterion is met. While this idea results in ROMs with small m, it requires a separate ROM construction (i.e., computation of influence functions and coefficient tensors) for each material point in the macroscopic domain, which is also computationally expensive.

2.3 Effective rotation of microstructure

In this manuscript, we propose an alternative methodology for a specific subset of microcracks that are most prone to the effects of load orientation. This methology is schematically illustrated in Fig. 2. Consider a reduced order model $\Re_{\Theta,S} = \{\mathbf{C}, \mathbf{D}, \mathbf{Z}\}$ of a microstructure, Θ, that induces a failure path, S with known orientation, $\mathbf{n}$ as shown in Fig. 2a. We consider that the failure path is aligned with a plane of statistical isotropy (i.e., the probability distributions describing the geometry are rotationally invariant, and that the microstructure is periodic, such as a hexagonal close-packed microstructure). It is then trivial to show that another ROM defined over the same microstructure but with a different failure path, $\hat{\Re}_{\Theta,\hat{S}} = \{\hat{\mathbf{C}}, \hat{\mathbf{D}}, \hat{\mathbf{Z}}\}$ shown in Fig. 2b is identical to the original model that undergoes a rigid body rotation, $\hat{\Re}_{\hat{\Theta},\hat{S}} = \{\hat{\mathbf{C}}, \hat{\mathbf{D}}, \hat{\mathbf{Z}}\}$ shown in Fig. 2c. The periodic boundary conditions are not affected by this rigid body rotation. The result implies that provided that a "reference" model with a known crack orientation is available, the reduced order model with any orientation with respect to the invariant plane could be constructed by simple tensor rotation operations. The transformation relationships are expressed as:

$$\begin{gathered} \hat{C}_{ijk} = R_{mi} R_{nj} R_{rk} C_{mnr} \\ \hat{D}_{ij} = R_{mi} R_{nj} D_{mn} \quad \hat{Z}_{ijk} = R_{mi} R_{nj} R_{rk} Z_{mnr} \end{gathered} \tag{9}$$

where $\mathbf{R}$ represents the transformation tensor under rotation. In random heterogeneous materials, such as isotropic concrete or particulate composites, the transformation tensor requires three Euler angles to describe the rotation. Since this manuscript focuses on long continuous fiber-reinforced composites, such a strategy is applicable to the matrix failure path whose crack plane is presumed to be parallel to the fiber direction (z-direction in Fig. 2). The transformation tensor can be then expressed as the angle of microstructural rotation θ in the transverse plane:

$$[\mathbf{R}(\theta)] = \\ [\cos(\theta), -\sin(\theta), 0; \sin(\theta), \cos(\theta), 0; 0, 0, 1] \tag{10}$$

2.4 Identification of crack orientation

In this study, we propose an identification criterion based on cohesive states in the failure path embedded in the microstructure after rotation. Before nucleation (i.e. $\kappa < \nu_c$), the traction variable $\mathbf{t}$ in the potential failure path is expressed as a function of the rotation angle θ

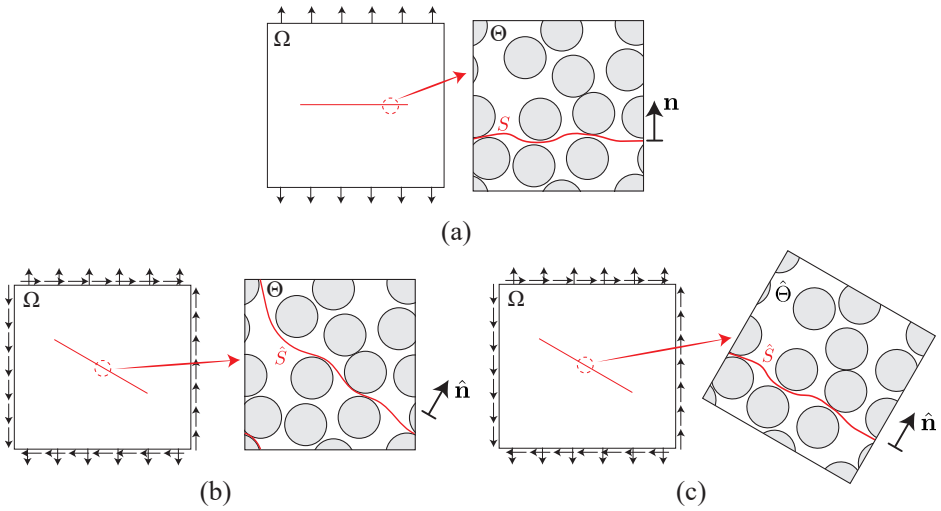

Fig. 2: Schematic illustration of different multiscale modeling strategies: (a) The microstructure and a predefined failure path; (b) the same microstructure with rotated failure path orientation; and (c) the rotated microstructure and the failure path adopted in this manuscript.

based on Eqs. 2 and 5:

$$\mathbf{t}(\theta) = \mathbf{K} \cdot [\mathbf{K} + \hat{\mathbf{D}}(\theta)]^{-1} \cdot \hat{\mathbf{C}}(\theta) : \bar{\boldsymbol{\epsilon}} \tag{11}$$

As shown in Fig. 3a, the traction state for different failure path orientations form an ellipsoid in the traction (t_N-t_T) space, where t_T represents the magnitude of the tangential traction: $t_T = \sqrt{t_{S1}^2 + t_{S2}^2}$. The quadratic failure initiation criterion shown in Eq. 6 defines an initiation envelop ($g = 0$) in the traction space which represents the peak strength as a function of mode-mixity. The intercept with horizontal and vertical axis respectively indicates pure mode-I condition: $t_N = t_{u_\mathrm{I}}$ and pure mode-II condition: $t_T = t_{u_\mathrm{II}}$. The encompassed region within the failure envelop defines the admissible traction states. The crack nucleates when the traction variable satisfies the failure criterion, denoted by the contact point between the traction curve and the initiation envelop. The failure path orientation at the contact point yields the nucleation direction θ_c, which satisfies:

$$\begin{cases} \mathbf{t}(\theta_c) = \mathbf{K} \cdot [\mathbf{K} + \hat{\mathbf{D}}(\theta_c)]^{-1} \cdot \hat{\mathbf{C}}(\theta_c) : \bar{\boldsymbol{\epsilon}} \\ g\big(t_N(\theta_c), t_T(\theta_c)\big) = 0 \end{cases} \tag{12}$$

while $g\big(t_N(\theta), t_T(\theta)\big) < 0$ if $\theta \neq \theta_c$.

In the numerical implementation of this methodology using an incremental scheme, identification of the exact contact point is not always possible. Consider that the microstructure is subjected to the macroscopic strain $\bar{\boldsymbol{\epsilon}}_n$ at time t_n within a discretized loading history $\{\bar{\boldsymbol{\epsilon}}_0, \bar{\boldsymbol{\epsilon}}_1, \ldots \bar{\boldsymbol{\epsilon}}_n \ \ldots\}$. At t_n, we define a trial traction curve that crosses into the initiation envelop, indicating that the softening stage is reached for a certain range of failure path orientations (indicated by the dashed portion of the curve in Fig. 3b). Since the traction curve in the previous increment remains within the initiation envelop, the failure path orientation needs to be identified at the current increment. Here, we consider that the nucleation direction is approximated by the failure path orientation that maximizes the criterion function g, which is computed by the elastic trial traction $\hat{\mathbf{t}}$. The trial traction is evaluated based on Eq. 11, assuming that the cohesive state is in hardening stage. The expression of the nucleation direction is:

$$\theta_c = \arg\max_{\theta} g\big(\hat{\mathbf{t}}(\theta)\big) \tag{13}$$

2.5 Numerical implementation

The overall implementation of the proposed multiscale approach consists of a preprocessing stage, where the reference reduced order model is constructed, and the multiscale analysis stage, where the multiscale reduced order system of equations are evaluated. The reference reduced order model is typically chosen to be the smallest representative volume or the unit cell that

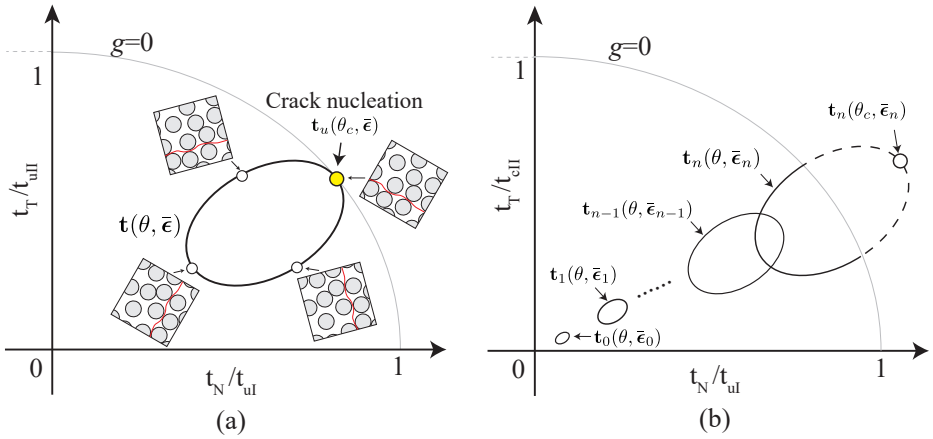

Fig. 3: Schematic illustration of identification criterion for nucleation direction in the normal-tangential traction space: (a) Nucleation direction θ_c denoted by the contact point between the traction state (black curve) and failure envelop $g = 0$ (light grey curve); (b) Nucleation direction defined in the trial state (black dash curve) which maximizes the criterion function g under discretized loading.

describes the microstructural geometry as discussed in Ref. [13]. Given the rotational invariance, the orientation of the reference failure path is arbitrary. The preprocessing stage consists of computing the coefficient tensors for the given microscopic geometry and the reference potential failure path. The preprocessing stage has been implemented using an in-house code [12]. The multiscale reduced order system of equations are evaluated in multiscale analysis stage, where the reference failure path is adaptively rotated at each macroscopic material point at the point of damage onset. Its implementation is performed using the commercially available finite element software, Abaqus. The evaluation of the reduced order microscale problem is performed using the user supplied subroutine functionality (i.e., UMAT).

The procedure for evaluation of the reduced order microscale problem consists of the following steps:

At initialization, assign the indicator NUCLEATED $\leftarrow$ 0 at each quadrature point indicating that the crack is not initiated. Assign the reduced order model at each quadrature point to be the reference reduced order model: $\mathfrak{R}^{\text{curr}} \leftarrow \mathfrak{R}_{\Theta,S}$.

During the multiscale simulation at a given increment, n at an arbitrary quadrature point, the macroscopic update procedure is as follows:

1. Update the homogenized strain: $\bar{\boldsymbol{\epsilon}}_n = \bar{\boldsymbol{\epsilon}}_{n-1} + \Delta\bar{\boldsymbol{\epsilon}}$.
2. If NUCLEATED = 0:

2a. Solve the optimization problem:

$$\min_{\theta} -g\big(\hat{\mathbf{t}}(\theta)\big),\ \theta \in [0, \pi] \tag{14}$$

where the trial traction variable is:

$$\hat{\mathbf{t}}(\theta) = \mathbf{K} \cdot [\mathbf{K} + \hat{\mathbf{D}}(\theta)]^{-1} \cdot \hat{\mathbf{C}}(\theta) : \bar{\boldsymbol{\epsilon}}_n \tag{15}$$

The trial failure path orientation is computed as the outcome of the optimization problem:

$$\hat{\theta} = \arg\max_{\theta} g\big(\hat{\mathbf{t}}(\theta)\big) \tag{16}$$

2b. If $g\big(\hat{\mathbf{t}}(\hat{\theta})\big) \geq 0$, the crack is initiated.

2b.1 Assign the indicator NUCLEATED $\leftarrow$ 1 and the nucleation orientation $\theta_c \leftarrow \hat{\theta}$.

2b.2 Compute trial rotation matrix $\hat{\mathbf{R}}$ using Eq. 10 with the nucleation orientation θ_c.

2b.3 Compute rotated reduced order model $\hat{\mathfrak{R}}_{\hat{\Theta},\hat{S}} = \{\hat{\mathbf{C}}, \hat{\mathbf{D}}, \hat{\mathbf{Z}}\}$ using the rotation transformation defined in Eq. 9.

2b.4 Assign $\mathfrak{R}^{\text{curr}} \leftarrow \hat{\mathfrak{R}}_{\hat{\Theta},\hat{S}}$

3. Compute reduced order traction variables $\mathbf{t}_n^{(\alpha)}$, separation variables $\boldsymbol{\delta}_n^{(\alpha)}$ and current damage state $\omega_n^{(\alpha)}$ by simultaneously solving Eqs. 2,4 and 5 using $\mathfrak{R}^{\text{curr}}$.
4. Update the macroscopic stress $\bar{\boldsymbol{\sigma}}_n$ using Eq. 3.

At step 2a, the optimization problem in Eq. 14 is solved using the golden section search approach [32]. It is a robust gradient-free numerical method for finding the minimum of an one-dimensional convex function on the

specified interval by successively narrowing the range of the parameter (i.e., θ) using the golden ratio. At step 3, the governing system of equations in the reduced-order model (Eqs. 2,4 and 5) is evaluated using the Newton-Raphson method.

3 Unit cell analysis

A series of unit cell analyses is performed to verify the adaptive MDDT model in capturing the failure behavior at the microscopic scale under multiaxial loading conditions. The microstructure configuration is shown in Fig. 4a. The fiber volume fraction is 28 %, and the fiber is aligned with the z direction. The hexagonal fiber arrangement ensures that the microstructure is rotationally invariant in the transverse (x-y) plane. The reference failure path for matrix cracking resides within the matrix constituent and wraps around the fiber. The average unit normal $\mathbf{n}$ of the failure path is parallel to the y-axis in the global coordinates. Elastic properties of the isotropic matrix and transversely isotropic fiber, and the fracture properties of matrix cracking failure path are listed in Table 1.

The macroscopic specimen and its boundary conditions are displayed in Fig. 4c. The specimen is restrained in fiber (z) direction in order to approximate plane strain conditions. In the following examples, three different monotonic strain-controlled loadings are applied in the transverse plane x-y.

Case 1. Combined tensile and simple shear loading: $\bar{\gamma}_{xy} = 2\bar{\epsilon}_{yy} > 0$.
Case 2. Simple shear loading: $\bar{\gamma}_{xy} > 0$.
Case 3. Combined biaxial tensile and simple shear loading: $\bar{\gamma}_{xy} = \bar{\epsilon}_{yy} = 0.625\bar{\epsilon}_{xx} > 0$.

The accuracy characteristics of the proposed model are compared with the reference direct numerical simulations (DNS) which resolve the microstructure and employ cohesive zone modeling (CZM) to track nucleation and propagation of the cracks. Because modeling 3D CZM is computationally expensive, the specimen for DNS is considered to be two-dimensional under plane strain condition. Two hexagonal unit cells form the domain for visual clarity of crack formation. The periodic boundary conditions are respectively applied to the DNS specimen for the three loading cases as shown in the following equations:

$$\begin{aligned} \mathbf{u}(x, L_y, z) - \mathbf{u}(x, 0, z) &= (\bar{\gamma}_{xy}\mathbf{i} + \bar{\epsilon}_{yy}\mathbf{j})\, L_y \\ \mathbf{u}(0, y, z) - \mathbf{u}(L_x, y, z) &= \bar{\gamma}_{xy} L_x \mathbf{j} \end{aligned} \tag{17}$$

$$\begin{aligned} \mathbf{u}(x, L_y, z) - \mathbf{u}(x, 0, z) &= \bar{\gamma}_{xy} L_y \mathbf{i} \\ \mathbf{u}(0, y, z) - \mathbf{u}(L_x, y, z) &= \bar{\gamma}_{xy} L_x \mathbf{j} \end{aligned} \tag{18}$$

$$\begin{aligned} \mathbf{u}(x, L_y, z) - \mathbf{u}(x, 0, z) &= (\bar{\gamma}_{xy}\mathbf{i} + \bar{\epsilon}_{yy}\mathbf{j})\, L_y \\ \mathbf{u}(0, y, z) - \mathbf{u}(L_x, y, z) &= (\bar{\epsilon}_{xx} + \bar{\gamma}_{xy}\mathbf{j})\, L_x \end{aligned} \tag{19}$$

where L_x, L_y, L_z respectively stand for the edge length at x, y, z directions, $0 \le x \le L_x$, $0 \le y \le L_y$, $0 \le z \le L_z$, $\mathbf{i}, \mathbf{j}$ are unit vectors consistent with global coordinate directions. The DNS domain is discretized with 4-noded bilinear quadrilateral elements (Fig. 4d). COH2D4 elements from ABAQUS cohesive element library are inserted to each face of every element within the matrix phase and the matrix-fiber interface. As the results below indicate, we do not observe a significant artificial compliance effect in the response due to the presence of cohesive elements along all solid element edges. The cohesive stiffness is set to 6×10^4 GPa/mm.

The simulations are run on an Intel Xeon Gold 6130 workstation with 16 cores, 2.10 GHz and 192 GB RAM. The proposed model uses single core for the simulations and the wallclock time for computation is 3s, orders of magnitude faster compared to DNS, which spends respectively 13,901s, 99,729s, 10,387s for the three cases using 16 cores with parallel computing.

The orientation of the reference failure path is set as $\theta = 0$. Positive θ represents counter-clockwise rotation of the microstructure. Figure 5 shows the comparison of the simulation results as computed using the DNS and the proposed multiscale simulations. The crack orientations (i.e. nucleation direction) obtained by the adaptive MDDT model are respectively $150°, 135°, 120°$ under the three loading cases. The first column of the figure shows the crack patterns predicted by DNS. In each case, a distinct crack forms within the microstructure, along with some additional damage that occurs prior to the onset of the dominant microcrack. The second column of the figure shows the traces of the dominant microcrack as the cohesive elements that has undergone full decohesion. The overall crack orientations observed in DNS show good agreement with the MDDT model predictions. Fig-

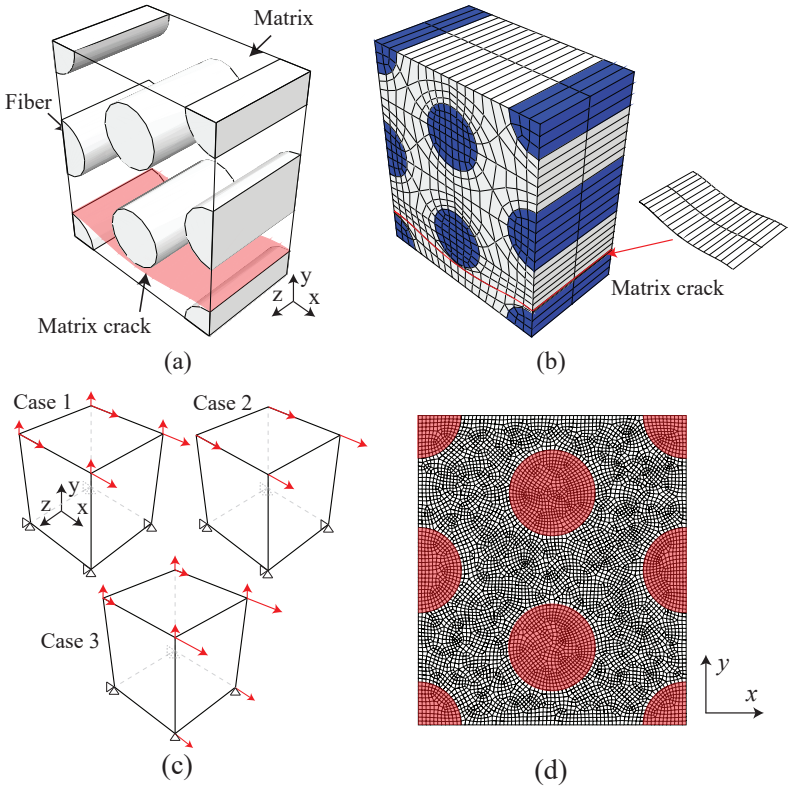

Fig. 4: (a) The hexagonal microstructure embedded with the failure path for matrix cracking. (b) Discretizations of the microstructure and failure path. (c) The macroscopic domain as well as the loading and boundary conditions for the unit cell tests using MDDT model. (d) Geometry and discretization of the 2D specimen for direct numerical simulations.

Table 1: Material properties of the composite constituents

Elastic properties of matrix$^{(m)}$ and fiber$^{(f)}$						
$E^{(m)}$	$\nu^{(m)}$	$E_1^{(f)}$	$E_2^{(f)}$	$G_{12}^{(f)}$	$G_{13}^{(f)}$	$\nu_{31}^{(f)}$
[GPa]		[GPa]	[GPa]	[GPa]	[GPa]	
4.67	0.34	280	17	5.67	30	0.3
Fracture parameters of matrix cracking for unit cell analysis						
G_{Ic}	G_{IIc}	t_{uI}	t_{uII}	K	η	
[MPa mm]	[MPa mm]	[MPa]	[MPa]	[MPa mm^{-1}]		
0.006	0.06	60	90	6×10^7	2.1	

ure 5 also displays the comparison of overall stress-strain responses between adaptive MDDT and DNS. A reasonable overall agreement is observed between the proposed reduced order model and the DNS from the aspects of peak strength and the trends of stress evolution after the peak strength. The overall shear stress-strain curves for Case 2 predicted by both the multiscale and the DNS simulations do not show a softening behavior due to the imposed boundary conditions. The boundary effects associated with periodicity constraints also cause some stress oscillations in the DNS simulations. Crack propagation is slightly disrupted when the dominant crack reaches the domain boundaries. An increase in tangent stiffness accompanied by a slight shift of the crack (circled in Fig. 5) as it propagates across the domain boundary. Furthermore, the proximity to fiber along the path of the microcrack results in some fluctuation of the slope of the overall stress-strain behavior

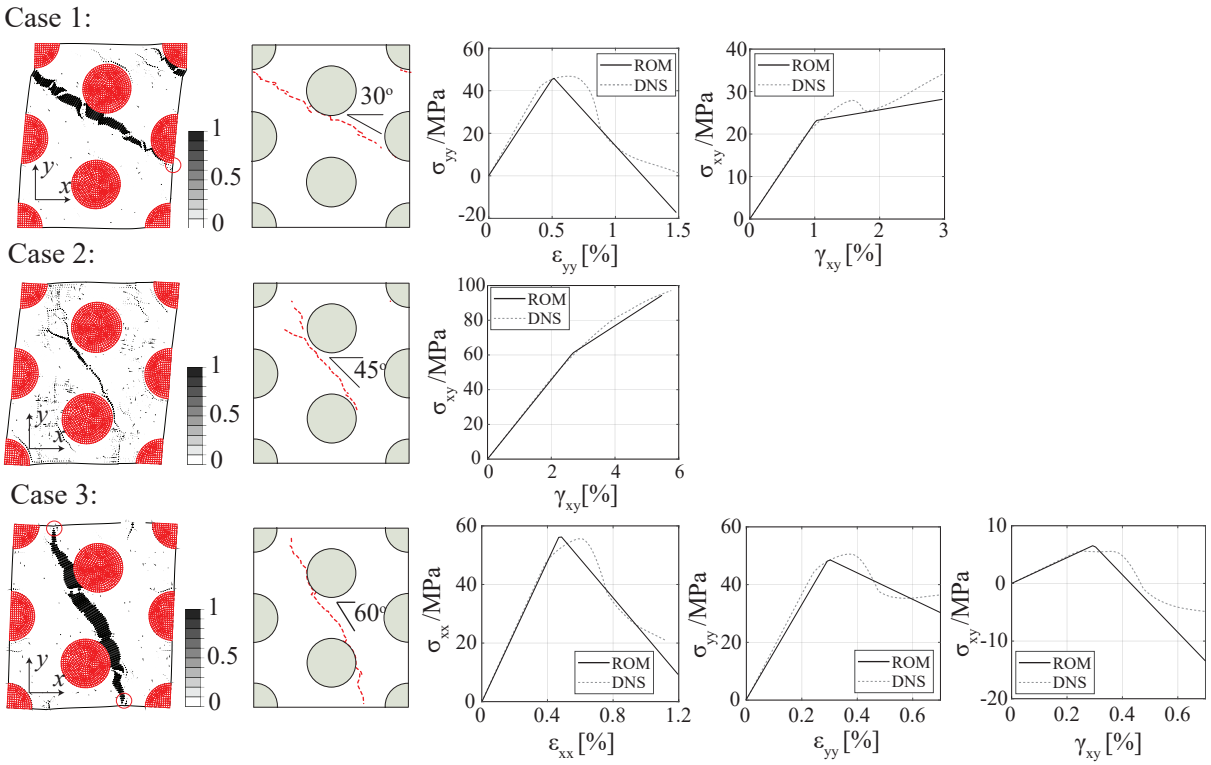

Fig. 5: Damage contours and crack paths in direct micro-mechanical numerical simulations, and comparison of stress-strain responses between MDDT model and direct numerical simulation under the strain loading conditions of case (1): $\bar{\gamma}_{xy} = 2\bar{\epsilon}_{yy} = 3\%$, case (2): $\bar{\gamma}_{xy} = 6\%$, and case (3) $\bar{\gamma}_{xy} = \bar{\epsilon}_{yy} = 0.625\bar{\epsilon}_{xx} = 0.7\%$.

in the DNS. These effects are not resolved in the multiscale model, as the MDDT model presumes uniform damage evolution within the failure path. A higher order MDDT model that resolves the crack growth within the microstructure could provide a more accurate match with the DNS. This could be achieved by considering multiple reduced order basis functions per failure path. This extension is nontrivial since separation field continuity along the failure path may need to be satisfied, and hence beyond the scope of this study.

3.1 Crack orientation and failure mode analysis

This section presents the effect of multiaxial strain-controlled loading on the orientation of the crack and the associated fracture mode. Here, we adopt the definition of crack nucleation orientation based on Eq. 12 (See Fig. 3a). Figure 6a,b shows the initiation conditions under three load configurations, Cases 1 to 3 as described above. In Fig. 6a, the critical traction states as a function of microcrack orientation at the point of failure initiation are shown by the elliptic curves in the traction space. Under pure shear or shear-tensile loading, the traction curves reach the initiation envelop (shown as the $g = 0$ isocontour) at the horizontal axis, indicating that the interface is in pure mode-I condition. Figure 6b shows the criterion function as a function of traction states at a given orientation. For a given loading condition, the critical orientation at which microcrack forms corresponds to the orientation where the criterion function reaches 0. In Cases 1 to 3, the critical orientation is unique and equals to $150°, 135°, 120°$, respectively.

Next, we further investigate the mode of failure and microcrack orientation under more general loading conditions. Figure 6c displays the overall crack orientation pattern as a function of multiaxial loading in the transverse plane (x-y plane). The x-axis of the contour stands for the ratio between shear and tensile strain component $\bar{\gamma}_{xy}/\bar{\epsilon}_{yy}$, while y-axis stands for the ratio between the two normal strain components $\bar{\epsilon}_{xx}/\bar{\epsilon}_{yy}$ (with $\bar{\epsilon}_{yy} > 0$). The contours in the figure are the isolines of crack orientation in $\bar{\gamma}_{xy}/\bar{\epsilon}_{yy}$ - $\bar{\epsilon}_{xx}/\bar{\epsilon}_{yy}$ space, satisfying $\bar{\epsilon}_{xx} - \bar{\epsilon}_{yy} + 2\cot 2\theta_c\ \bar{\gamma}_{xy} = 0$. The isolines set out from the point

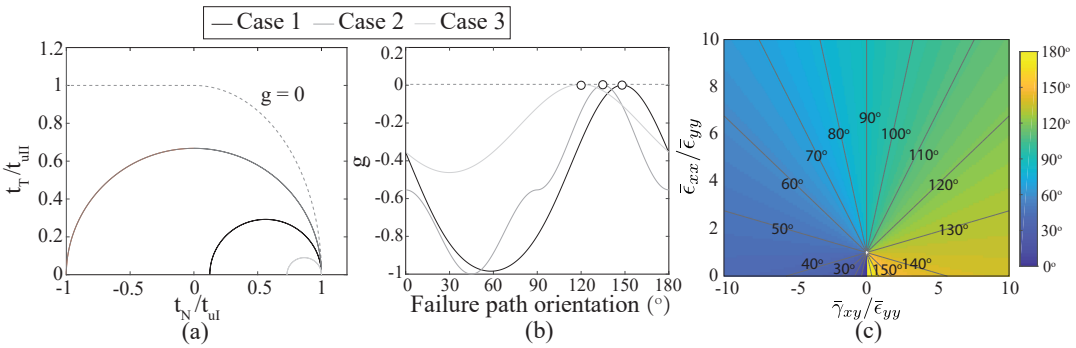

Fig. 6: (a) The traction states in t_N-t_T space when reaching the initiation envelop under the strain loading conditions in the transverse plane. (b) The corresponding criterion function as a function of traction states at a given orientation. (c) Contours of crack orientation under multi-axial strain loading conditions within the transverse plane.

$\bar{\epsilon}_{xx} = \bar{\epsilon}_{yy}$, representing the pure hydrostatic state where the failure initiates at all directions at once. It is easy to verify that the isoline of crack orientation overlaps with the direction of maximum macroscopic principal stress, consistent with the classical failure criterion for brittle or quasi-brittle materials (see e.g. [33, 34]). In addition, all cracks represented in Fig. 6c initiate under mode-I conditions.

Next, we investigate failure initiation when the loading is not within the transverse plane. Figure 7a displays the traction state (denoted by solid line) for the failure initiation within the failure path parallel to the fiber (denoted as in-plane failure path) under the in-plane shear loading (case 4: $\bar{\gamma}_{yz} > 0$). The traction reaches the initiation envelop under pure mode-II at the orientation of $\theta_c = 0°$ (denoted by circle mark). Another traction state (denoted by star mark) is shown in Fig. 7a under the same loading but within the failure path which is 45° across the fiber (denoted as out-of-plane failure path), consistent with direction of maximum macroscopic principal stress. The traction is outside the initiation envelope under approximate mode-I condition, indicating that the mode-I crack initiates prior to the in-plane failure path which initiates under mode-II condition. We further note that mode-I out-of-plane fracture occurs only slightly before a possible mode-II in-plane fracture. This indicates that both of the failure states are possible depending on the microscopic geometry and failure properties associated with mode-I and mode-II fracture. These two mechanisms have been experimentally observed and well known. The crack parallel to the fiber is a splitting crack which is commonly seen in the notched laminates subjected to tensile loading [35]. The crack crossed by the fiber indicates shear matrix cracks, which have been observed in the off-axis laminates under tension [36]. The cross-fiber fracture plane associated with the mode-I failure (star mark in Fig. 7) is not rotationally invariant, and therefore the adaptive strategy can only accurately capture the mode II in plane fracture case. A hybrid strategy is necessary to track both failure modes, where the adaptive strategy is used to track in-plane failure modes, whereas additional paths are a-priori inserted to capture behavior in non-invariant orientations.

Figure 7b displays the traction states within a in-plane failure path under the loadings of Cases 4-6. In Case 5, the combination of $\bar{\epsilon}_{yy}$ and $\bar{\gamma}_{yz}$ results in mixed-mode failure but the same nucleation direction as Case 4, $\theta_c = 0°$. Case 6 represents a more complex situation as $\bar{\gamma}_{xy}$ is involved, in which the crack nucleates at tilted direction ($\theta_c = 158°$) under mixed-mode condition.

4 Four-point bending beam analysis

The proposed model is further verified by predicting the crack propagation in notched concrete beam specimens with four-point constraints. The numerical results are compared with the experiments described in Ref. [18]. Figure 8a shows the particle microstructure configuration employed for concrete. Statistical isotropy is ensured for the rotational plane within the microstructure in the three dimensional space. The volume fraction of aggregate particles is 32% and the radius of spherical idealized particles is 5 mm. The modulus of the ag-

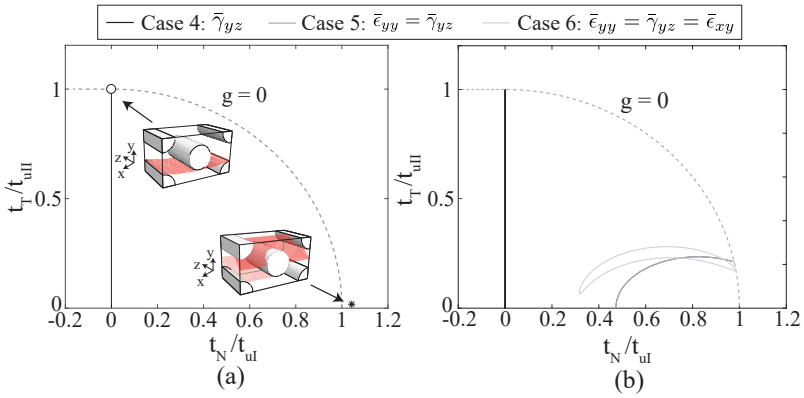

Fig. 7: The traction states in t_N-t_T space (a) for the matrix failure paths parallel to fiber and 45° across the fiber under in-plane shear loading ($\bar{\gamma}_{yz}$) (b) for the matrix failure paths parallel to the fiber under combined tensile and in-plane shear loading.

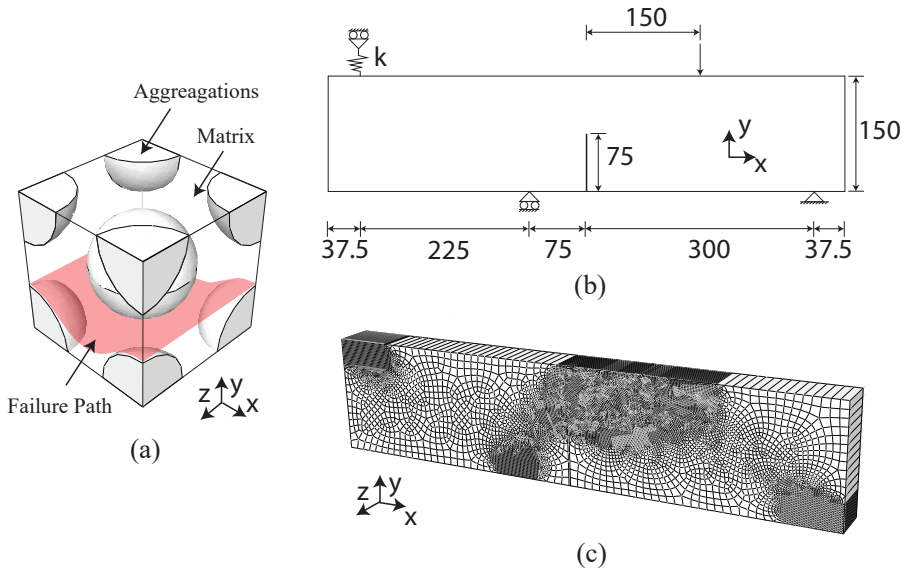

Fig. 8: (a) Microstructure configuration of concrete material (b) Geometry and boundary conditions of four-points bending specimen test. (c) Numerical model and mesh discretizations.

gregate and the cement are respectively 50 GPa and 34 GPa, and their Poisson's ratio are 0.2. The resulting homogenized modulus (38 GPa) and Poisson's ratio (0.2) are consistent with the concrete properties in Ref. [18]. The tensile strength and fracture energy of the cement cracking failure path are respectively 0.4 MPa and 0.06 MPa·mm for both mode-I and mode-II. Figure 8b shows the specimen geometry and boundary conditions. The thickness of the specimen in z-direction is 50 mm. A displacement-controlled loading is applied at the top (Fig. 8b). The numerical specimens are respectively restrained by two types of boundary conditions (named type-1 and type-2) which result in different crack trajectories. The vertical spring stiffness imposed at top left position is respectively set to be $k = 0$ (free boundary) and $k = \infty$ (vertical displacement restrained) for type-1 and type-2 boundary conditions. The rest of boundary conditions are the same in the two cases. Because no external loading is added along the out-of-plane direction (z direction), the particulate microstructure is considered to perform effective rotation only in x-y plane. Figure 8c displays the mesh discretization, wherein 8-noded tri-linear hexahedral elements are

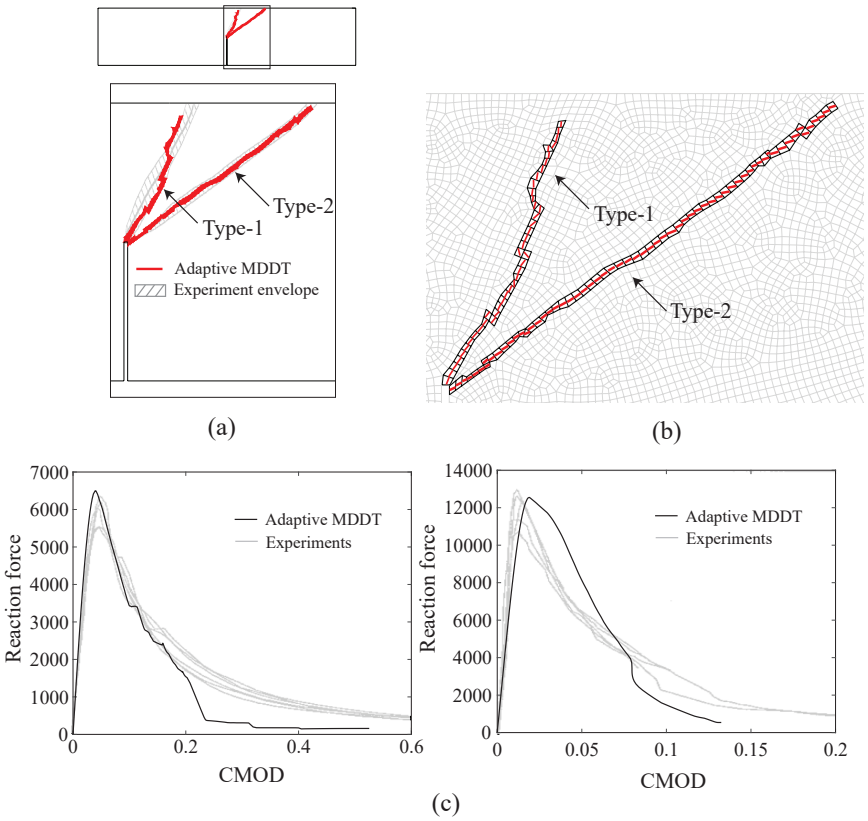

Fig. 9: (a) Macrosopic crack path of type-1 and type-2 boundary conditions. (b) Element-wise microcrack orientation (denoted by direction of red line) for type-1,2 cases. (c) CMOD vs. reaction force at loading position for type-1 (left) and type-2 (right) cases.

employed for discretization with reduced integration and hourglass control.

The numerical results of both type-1 and type-2 boundary conditions are shown in Fig. 9, wherein Fig. 9a displays the completely cracked elements (with damage variable $\omega = 1$) in the domain obtained by the proposed model. The macrocrack propagations in type-1 and 2 cases respectively reveal the direction towards 67° and 36° with respect to horizontal and overlap with experimental crack path envelop. Figure 9b displays the corresponding element-wise microscopic crack orientation, denoted by direction of red lines within the mesh discretization. There is clearly an overall consistency of microcrack orientation with the trend of macrocrack propagation direction. Some deviations occur for type-2 case as crack growth approaches the top edge, wherein the mesh alignment obstructs macrocrack from following the microcrack orientation in a smaller angle (10° - 20°) with respect to horizontal. Figure 9c,d respectively show the responses of CMOD (i.e. crack mouth opening displacement) vs. reaction force at loading position for type-1 and type-2 case. Type-1 displays a very reasonable match with experiment results until a sudden drop of force response, which indicates the crack propagation near the top edge of the specimen. There is an overall agreement between type-2 case and experiments as well, also with a force drop as crack approaches the top of the specimen.

5 Delamination migration modeling

Delamination migration is a typical kind of re-orienting crack in fiber reinforced composites. It is associated with local micro crack accumulation at the delamination front, which results in kinking failure when the crack reorientation is energetically favorable to delamination propagation [34]. The propagation of the kinked crack typically reverts to delamination growth at another ply interface if arrested by the fibers. Numerical modeling

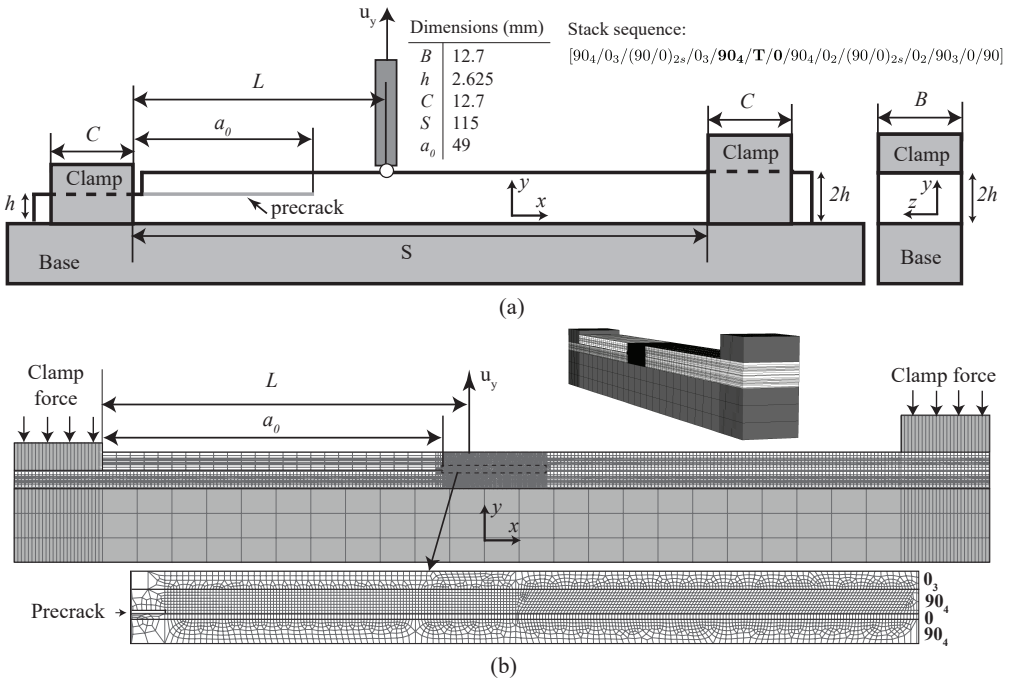

Fig. 10: (a) Geometry sketch of cross-ply tape laminates in the delamination migration test. (b) Numerical model and mesh discretizations. Inset figure displays the structured mesh discretization for potential delamination propagation.

Table 2: Homogenized elastic moduli of the composite and fracture properties used in the delamination migration model

$E_{11} = E_{22}$	E_{33}	$G_{12} = G_{13}$	G_{23}	$\nu_{12} = \nu_{13}$	ν_{23}
[GPa]	[GPa]	[GPa]	[GPa]		
9	156	2.99	5.08	0.49	0.32
Fracture parameters of matrix cracking for unit cell analysis					
G_{Ic}	G_{IIc}	t_{uI}	t_{uII}	K	η
[MPa mm]	[MPa mm]	[MPa]	[MPa]	[MPa mm^{-1}]	
0.2	1	60	90	6×10^7	2.1

of delamination are typically performed using virtual crack closure technique (VCCT) or cohesive zone modeling (CZM) [37]. For modeling re-oriented kinking crack, such approaches have been combined with continuum damage modeling (CDM) (e.g. [33]) or element enrichment strategies such as extended finite element method (xFEM) (e.g. [38]) or floating node method (FNM) (e.g. [34]). In this section, the proposed reduced order multiscale model is employed for delamination migration modeling using cross-ply laminates configuration and validated with a series of delamination migration experiments [19].

5.1 Numerical model

The cross-ply specimens employed in this section were experimentally investigated in Ref. [19]. All constituent properties are identical to those used in the previous section and listed in Table 1. Hexgonal packed microstructure with fiber volume fraction of 55% is employed in this section. The corresponding homogenized stiffness is consistent with IM7/8552 carbon fiber-epoxy composite [33, 39] and shown in Table 2, along with the fracture properties employed for both intralaminar matrix cracking and delamination. Depending on the processing conditions, lamina interfaces could be more resin-

rich and exhibit homogenized fracture properties that differ from intralaminar matrix cracking [40]. In this study, we assume that the fracture properties within the lamina and at the interfaces are taken to be the same [41]. Figure 10a displays the test configuration and the ply layup. The span length, width and thickness of the specimen are 115mm, 12.7mm, 5.25mm, respectively. A precrack (denoted by **T** for teflon in the layup shown in Fig. 10) is inserted between $90_4/0$ interface and its length a is 49mm. The specimens are subjected to vertical displacement-controlled loading applied at four different positions at the top surface, represented by the load offsets $L/a = 1, 1.1, 1.2, 1.3$, where L is the distance from the loading position to the left tip. The specimen is clamped to the fixture at both ends.

Figure 10b shows the finite element mesh of the specimen (i.e., the macroscopic domain) and the fixture. 8-noded tri-linear hexahedral elements with reduced integration and hourglass control are employed for the discretization. The plies with different orientations are modeled as separate layers of elements. In the z-direction (through the plane), the ply is discretized with one layer of elements. The delamination growth and potential migration region $(\ldots 90_4/\mathrm{T}/0\ldots)$ is discretized by a structured mesh. The precrack is embedded in 90°_4 ply, as shown in Fig. 10b. The thickness of the pre-crack is set to 6 μm, which is the same as the teflon insert thickness. A row of elements of the same width as the precrack are placed ahead of the precrack to ensure that delamination propagation would proceed without mesh effects. Within the rest of the central 90° ply block, element edges are oriented 60° to the horizontal (x) direction to minimize mesh bias effect as the migration is expected to occur approximately at this angle [19]. The effect of mesh orientation is further discussed below. The numerical modeling of the fixture is the same in Ref. [34]. Constraints are applied to the two ends of the specimen via rigid contact condition with friction between clamp fixture, base plate and the specimen. A clamping force of 1,700N is added on the fixture via two reference nodes whose displacements are coupled with the top nodes on the fixture. The clamping force is applied in the initial step before adding the vertical load at the load offset positions. The stiffness of the fixture is 6.8 GPa and its Poisson's ratio is 0.34. The friction coefficient is set to 0.2. The displacement at the bottom of the base plate is fixed at all directions.

5.2 The results for different load offsets

Figure 11a-d show the force-displacement responses predicted for different load offsets and compared with experimental observations. The beginning of the first unstable event (denoted by circle 0) represents the onset of delamination propagation, which continues as the specimen unloads. The stiffness and the peak strength have overall reasonable agreements with the experimental results. The second loading stage is associated with the migration event. Figure 12 shows the damage contours at the end of the simulations for each load case. A thin yellow line in an element indicates that the failure path within the microstructure has been set (i.e., initiation criterion has been met), and the failure path has undergone partial damage ($0 < \omega < 1$). Elements with a red line indicates that complete debonding has occurred ($\omega = 1$). The line orientation indicates microcrack direction. Figure 12 also displays the corresponding position of the crack tip for the beginning (circle 1) and ending point (circle 3) of the second loading stage in the load-displacement curve. During the unstable propagation stage associated with the first load drop (between circle 0 and 1), the delamination propagates along the 90°/0° ply interface without change in the microcrack orientation. The second loading stage (between circles 1 and 2) is associated with the formation of a process zone around the crack tip, as evidenced by the presence of partially damaged microcracks. At this stage, the dominant crack also progressively changes direction and respectively aligns with approximately 50 degree angle for the cases of $L/a = 1, 1.2, 1.3$ and 45 degree angle for $L/a = 1.1$ at the location of circle 2. The model predicts a rather sudden migration event with insignificant change in load (from circle 2 to 3), which is followed by the second unstable event. Delamination propagation at the upper 90°/0° ply interface occurs during the second load drop. As shown in Fig. 12, the microcracks reorient to align with the ply interface prior to the propagation of the migrated delamination. The analysis of the initiation as well as the traction-separation conditions that form the dominant crack indicates that the fracture process is largely mode I.

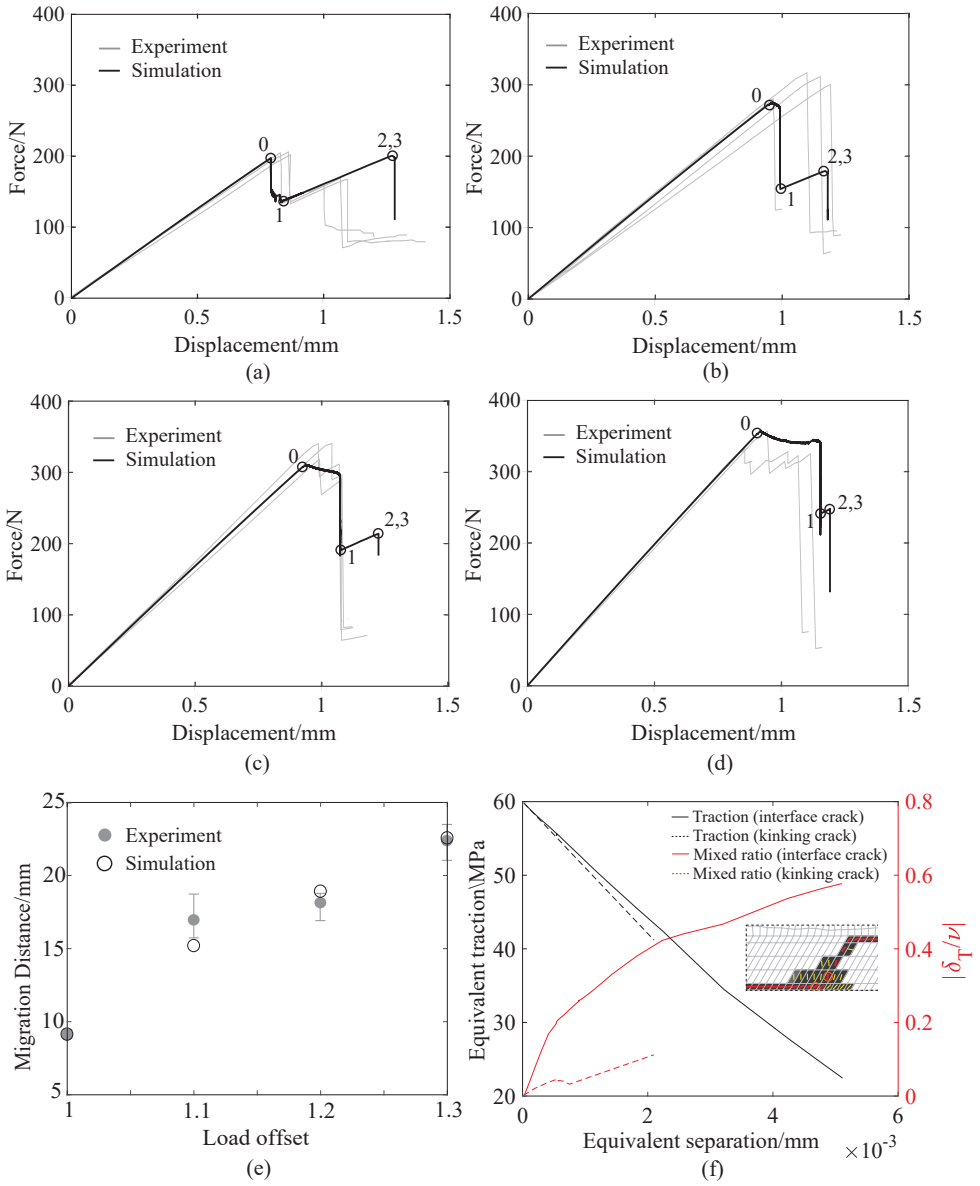

Fig. 11: Force displacement curves for different load offsets (a) $L/a = 1$, (b) $L/a = 1.1$, (c) $L/a = 1.2$, (d) $L/a = 1.3$. (e) Migration distance vs. load offset. (f) Equivalent traction (solid lines) and mode mixity (dash lines) as a function of equivalent separation extracted from the elements in interface crack and kinking crack for $L/a = 1.1$. The location of the elements are indicated in the inset damage contour.

The features of the predicted force-displacement curve are in agreement with experimental observations in the case of $L/a = 1$ (See Fig. 11a and [19]). The larger load offset cases do not show a second loading stage, where the entire process occurs under unstable conditions. The simulations also show a progressively smaller stable reload region, which nearly disappears when $L/a = 1.3$. A possible explanation of this discrepancy is that fixing the crack orientation at the onset of interface failure overconstrains the material at the fracture process zone. While the subscale (i.e., unresolved) damage events at the fracture process zone are more aligned with the proposed criterion, load redistribution may result in a further realignment prior to percolation. Some theories adjust crack orientation even after nucleation [33, 42, 43], but enhancement of the current methodology to account for such an effect is nontrivial and outside the scope of this study.

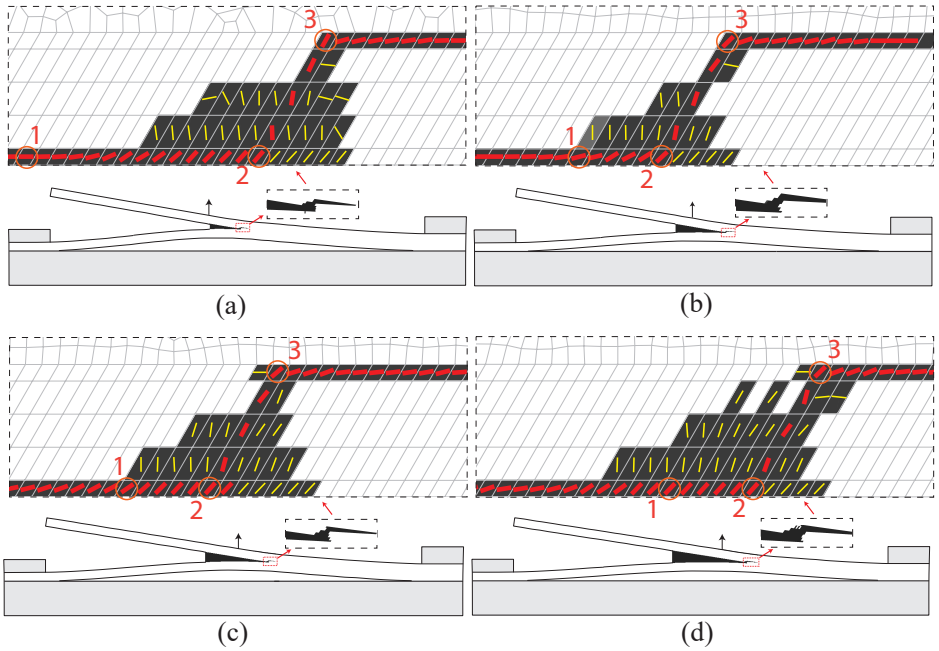

Fig. 12: Damage contours of delamination and kinking failure around the migration location for the load offset (a) $L/a = 1$, (b) $L/a = 1.1$, (c) $L/a = 1.2$, (d) $L/a = 1.3$. The crack orientation is marked by lines within the elements, wherein thin yellow ones stands for micro crack ($0 < \omega < 1$) and thick red ones for complete crack ($\omega = 1$).

Figure 11e shows the distance from the precrack tip to the onset of migration crack (i.e. migration distance) as a function of load offsets. The increasing trend of migration distance with normalized load offset agrees well with the experiments. The shifting of the migration distance as a function of load offset (or more specifically, L) has been explained by the shift in the location in the specimen, where the shear stress ahead of the crack tip changes sign [19, 34]. During the delamination propagation stage, the shear stress is positive and the microcracks tend to form with a downward trend. This action is resisted by the 0° ply below the crack, and the delamination pre-crack extends horizontally. The magnitude of the shear stress reduces with the crack growth. As shown in Fig. 6c, the microcracks turn progressively in the clockwise direction with a reduction in shear stress and kink upwards when the shear stress becomes negative. The simulations confirm the change in sign of shear stress at onset of the migration process, which agrees well with observations made in Ref. [19, 44]. Experiments also indicate a gradual kinking of the macrocrack (a smooth transition to the migration crack) before the migration event. In the current numerical simulations, mesh bias effects do not permit a gradual crack reorientation, but this propensity manifests itself as the formation of the fracture process zone near the migration location. While the extent of the process zone is exacerbated by the numerical effects of mesh bias and due to setting of the microcrack orientation at failure onset, presence of a fracture process zone has been observed experimentally in Ref. [44] as well. Those delamination tests show multiple migration attempts that fail to crack through the lamina before the migration event.

Figure 11f extracts the equivalent traction (denoted as $\|\mathbf{t}\| = \sqrt{t_N^2 + t_{S1}^2 + t_{S2}^2}$) and mixed-mode ratio (denoted by $|\delta_T/\nu|$) resolved in the softening stage as a function of equivalent separation (ν) from the elements respectively within the interface crack and the kinking crack near the migration location in the $L/a = 1.1$ case. The curves of mixed mode ratio show that the interface crack (denoted by dash line) nucleates under mode-I condition but gradually involves mode-II fracture in the softening stage, while there is not much shear deformation in the kinking crack (denoted by dash line). The feature is consistent with fractography observations in Ref. [19].

5.3 The effect of mesh discretization

The influence of mesh alignment on the migration behavior is also investigated. Figure 13a shows the result of $L/a = 1.1$ using a fully structured mesh with vertical mesh alignment. We observe that there is initiated damage with reorientation (denoted by yellow lines) in the 90° ply but the mesh alignment prevents the migration event and the delamination continuously propagates along the initial interface. Another simulation case employs the mesh edge orientation of 45° with respect to the x direction. The damage pattern, microcrack orientations and the force-displacement response (See Fig. 13g) are similar to those obtained with the 60° mesh. The dominant crack reorients at 45° before complete migration crack occurs. The migration distance is 15.05mm, very close to the 15.19mm predicted by the mesh with 60° alignment.

A mesh size convergence study for kinking failure is also performed. Additional simulations with element sizes of 4mm, 3mm, 2mm in both x and y directions are performed with the load offset $L/a = 1.1$. The mesh edge orientation is set to 60° with respect to the x direction. Mesh size regularization is performed using the procedure explained in Ref [12]. Figures 13c-f show the damage contours and the crack orientation for different mesh densities. Displaying the same part of the specimen, the contours show that the migration locations have almost no change with the mesh size. The orientation of the complete kinking failure is around 60° near the initial interface and gradually becomes near horizontal when it approaches the second interface. It is more clearly shown in Fig. 13f that the orientation converges around 20° to 30° as the mesh size decreases. Figure 13g displays the force-displacement responses for different mesh densities, which shows good agreement with each other except for the slight discrepancies of the peak points for the second unstable event.

6 Conclusion

This paper introduced an adaptation of MDDT to model the multiscale evolution of fracture in composite materials, when the cracks tend to kink under evolving loading and geometric conditions. The idea of rotating the microstructure to capture correct microcrack orientation drastically reduces the number of potential failure paths and consequently increases the computation efficiency. With this approach, we were able to investigate microscopic and macroscopic fracture conditions of reorienting crack. It is important to note that the efficiency gains are in modeling fracture paths in rotationally invariant microstructures, or along planes within microstructure that exhibits rotational invariance. In generalized microstructures, establishing a hybrid strategy, where multiple failure paths are introduced along planes that do not exhibit rotational invariance, and the microstructure rotation idea is used in rotationally invariant planes could accurately characterize fracture under multiaxial loading.

Another important observation made is that under identical loading conditions, multiple failure paths may exist with similar critical conditions. Under pure shear, mode II splitting cracks and mode I matrix cracks exhibit very similar initiation strength. Given this similarity, microstructural features may dictate which of these mechanisms prevail, highlighting the multiscale nature of the problem.

7 Acknowledgements

The authors gratefully acknowledge the financial support of the Office of Naval Research Airframe Structures and Materials (Award No: N00014-17-1-2040, Program Manager: Dr. Anisur Rahman). We also gratefully acknowledge Dr. Nelson Carvalho for sharing the details of the boundary conditions used in [34], and for his valuable feedback.

References

1. Tan SC, Nuismer RJ (1989) A Theory for Progressive Matrix Cracking in Composite Laminates. Journal of Composite Materials 23(10):1029–1047, DOI https://doi.org/10.1177/002199838902301006
2. Van Der Meer FP, Sluys LJ (2009) Continuum models for the analysis of progressive failure in composite laminates. Journal of Composite Materials 43(20):2131–2156, DOI https://doi.org/10.1177/0021998309343054

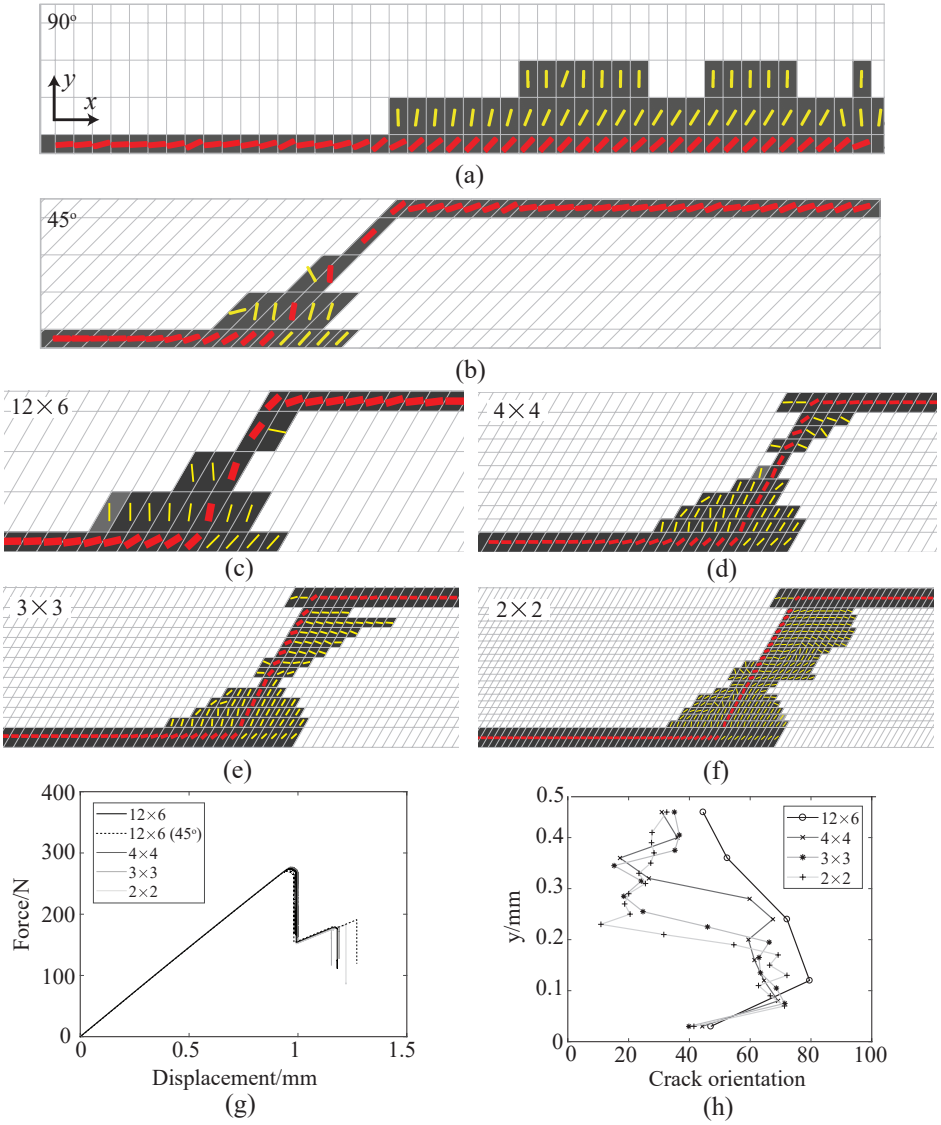

Fig. 13: Damage contours at the migration location for the load offset of $L/a = 1.1$ with different mesh alignment: (a) 90°, (b) 45°, and different sizes of mesh discretizations: (c) 6mm × 12mm, (d) 4mm × 4mm, (e) 3mm × 3mm, (f) 2mm × 2mm. (g) The force-displacement responses of different mesh sizes and alignment. (h) The crack orientation along the kinking crack ($\omega = 1$) from the bottom interface (y=0.03mm) to the top interface (y=0.45mm) across the 90_4 ply for different mesh sizes.

3. Tsai SW, Wu EM (1971) A General Theory of Strength for Anisotropic Materials. Journal of Composite Materials 5(1):58–80, DOI https://doi.org/10.1177/002199837100500106
4. Oskay C, Fish J (2007) Eigendeformation-based reduced order homogenization for failure analysis of heterogeneous materials. Computer Methods in Applied Mechanics and Engineering 196(7):1216–1243
5. Gong Y, Zhang B, Hallett SR (2018) Delamination migration in multidirectional composite laminates under mode I quasi-static and fatigue loading. Composite Structures 189:160–176, DOI https://doi.org/10.1016/j.compstruct.2018.01.074
6. Saliba J, Matallah M, Loukili A, Regoin JP, Grégoire D, Verdon L, Pijaudier-Cabot G (2016) Experimental and numerical analysis of crack evolution in concrete through acoustic emission technique and mesoscale modelling. Engineering Fracture Mechanics 167:123–137, DOI 10.1016/j.engfracmech.2016.03.044
7. Hu W, Ha YD, Bobaru F (2012) Peridynamic model for dynamic fracture in unidirectional fiber-

reinforced composites. Computer Methods in Applied Mechanics and Engineering 217-220:247–261, DOI https://doi.org/10.1016/j.cma.2012.01.016

8. Belytschko T, Loehnert S, Song JH (2014) Multiscale aggregating discontinuities: A method for circumventing loss of material stability. International Journal for Numerical Methods in Engineering 00(7):1–19, DOI https://doi.org/10.1002/nme.2156
9. Toro S, Sánchez PJ, Podestá JM, Blanco PJ, Huespe AE, Feijóo RA (2016) Cohesive surface model for fracture based on a two-scale formulation: computational implementation aspects. Computational Mechanics 58(4):549–585, DOI 10.1007/s00466-016-1306-y
10. Bogdanor MJ, Oskay C (2016) Prediction of progressive damage and strength of IM7/977-3 composites using the Eigendeformation-based homogenization approach: Static loading. Journal of Composite Materials 51(10):1455–1472, DOI https://doi.org/10.1177/0021998316650982
11. Oskay C (2009) Two-level multiscale enrichment methodology for modeling of heterogeneous plates. International journal for numerical methods in engineering 80(9):1143–1170, DOI https://doi.org/10.1002/nme.2652
12. Oskay C, Su Z, Kapusuzoglu B (2020) Discrete eigenseparation-based reduced order homogenization method for failure modeling of composite materials. Computer Methods in Applied Mechanics and Engineering 359:112656, DOI https://doi.org/10.1016/j.cma.2019.112656
13. Su Z, Oskay C (2021) Mesh size objective fatigue damage propagation in laminated composites using the multiscale discrete damage theory. Computational Mechanics 67(3):969–987, DOI https://doi.org/10.1007/s00466-021-01978-7
14. Coenen EWC, Kouznetsova VG, Geers MGD (2012) Multi-scale continuous-discontinuous framework for computational- homogenization-localization. Journal of the Mechanics and Physics of Solids 60(8):1486–1507, DOI https://doi.org/10.1016/j.jmps.2012.04.002
15. Xiaoyu Z, Oskay C (2019) Plastic dissipation sensitivity to mechanical properties in polycrystalline β-hmx subjected to impact loading. Mechanics of Materials 138:103079, DOI https://doi.org/10.1016/j.mechmat.2019.103079
16. Bogdanor MJ, Clay SB, Oskay C (2019) Interacting Damage Mechanisms in Laminated Composites Subjected to High Amplitude Fatigue. Journal of Engineering Mechanics 145(10):1–11, DOI 10.1061/(ASCE)EM.1943-7889.0001655
17. Xiang Z, Oskay C (2017) Sparse and scalable eigenstrain-based reduced order homogenization models for polycrystal plasticity. Computer Methods in Applied Mechanics and Engineering 326:241–269, DOI https://doi.org/10.1016/j.cma.2017.07.027
18. Gálvez JC, Elices M, Guinea GV, Planas J (1998) Mixed mode fracture of concrete under proportional and nonproportional loading. International Journal of Fracture 94(3):267–284, DOI 10.1023/A:1007578814070
19. Ratcliffe JG, M W Czabaj, O'Brien TK (2013) A test for chracterizing delamination migration in carbon/epoxy tape laminates. Tech. Rep. August 2013, NASA
20. Guedes JM, Noboru K (1990) Preprocessing and postprocessing for materials based on the homogenization method with adaptive finite element methods. Computer methods in applied mechanics and engineering 83(2):143–198, DOI https://doi.org/10.1016/0045-7825(90)90148-F
21. Geers MGD, Kouznetsova VG, Matouš K, Yvonnet J (2017) Homogenization Methods and Multiscale Modeling: Nonlinear Problems. John Wiley & Sons, Ltd, DOI https://doi.org/10.1002/9781119176817.ecm2107
22. Sparks P, Oskay C (2016) The method of failure paths for reduced-order computational homogenization. International Journal for Multiscale Computational Engineering 14(5):515–534, DOI https://doi.org/10.1615/IntJMultCompEng.2016018702
23. Dvorak GJ, Benveniste Y (1992) On transformation strains and uniform fields in multiphase elastic media. Proceedings: Mathematical and Physical Sciences 437:291–310, DOI 10.1098/rspa.1992.0062
24. Zhang X, Oskay C (2016) Polycrystal plasticity modeling of nickel-based superalloy in 617 subjected to cyclic loading at high temperature. Modelling and Simulation in Materials Science and Engineer-

ing 24(5):55009, DOI https://doi.org/10.1088/0965-0393/24/5/055009
25. Camanho PP, Dávila CG (2002) Mixed-mode decohesion finite elements for the simulation of delamination in composite materials. Tech. rep., NASA
26. Song SH, Paulino GH, Buttlar WG (2006) A bilinear cohesive zone model tailored for fracture of asphalt concrete considering viscoelastic bulk material. Engineering Fracture Mechanics 73(18):2829–2848, DOI 10.1016/j.engfracmech.2006.04.030
27. de Morais AB, Pereira AB, de Moura M, Silva F, Dourado N (2015) Bilinear approximations to the mixed-mode I-II delamination cohesive law using an inverse method. Composite Structures 122:361–366, DOI 10.1016/j.compstruct.2014.11.058
28. Benzeggagh ML, Kenane M (1996) Measurement of mixed-mode delamination fracture toughness of unidirectional glass/epoxy composites with mixed-mode bending apparatus. Composites Science and Technology 56(4):439–449, DOI https://doi.org/10.1016/0266-3538(96)00005-X
29. Govindjee S, Kay GJ, Simo JC (1995) Anisotropic modelling and numerical simulation of brittle damage in concrete. International Journal for Numerical Methods in Engineering 38(21):3611–3633, DOI https://doi.org/10.1002/nme.1620382105
30. Hoover CG, Bažant ZP (2014) Cohesive crack, size effect, crack band and work-of-fracture models compared to comprehensive concrete fracture tests. International Journal of Fracture 187(1):133–143, DOI 10.1007/s10704-013-9926-0
31. Oskay C, Su Z (2019) Prediction of Fatigue Failure in Fibrous Composites Using the Reduced-Order Multiscale Discrete Damage Theory. SAMPE 2019-Charlotte, NC, May 2019 DOI 10.33599/nasampe/s.19.1430
32. Press WH, Teukolsky SA, Vetterling WT, Flannery BP (1992) Golden section search in one dimension. Numerical Recipes in C: The Art of Scientific Computing p 2
33. Pham DC, Cui X, Ren X, Lua J (2019) A discrete crack informed 3D continuum damage model and its application for delamination migration in composite laminates. Composites Part B: Engineering 165:554–562, DOI https://doi.org/10.1016/j.compositesb.2019.02.045
34. De Carvalho NV, Chen BY, Pinho ST, Ratcliffe JG, Baiz PM, Tay TE (2015) Modeling delamination migration in cross-ply tape laminates. Composites Part A: Applied Science and Manufacturing 71:192–203, DOI https://doi.org/10.1016/j.compositesa.2015.01.021
35. O'Higgins RM, McCarthy MA, McCarthy CT (2008) Comparison of open hole tension characteristics of high strength glass and carbon fibre-reinforced composite materials. Composites Science and Technology 68(13):2770–2778, DOI https://doi.org/10.1016/j.compscitech.2008.06.003
36. Ng WH, Salvi AG, Waas AM (2010) Characterization of the in-situ non-linear shear response of laminated fiber-reinforced composites. Composites Science and Technology 70(7):1126–1134, DOI https://doi.org/10.1016/j.compscitech.2010.02.024
37. Tabiei A, Zhang W (2018) Composite laminate delamination simulation and experiment: A review of recent development. Applied Mechanics Reviews 70(3), DOI https://doi.org/10.1115/1.4040448
38. Hu XF, Chen BY, Tirvaudey M, Tan VBC, Tay TE (2016) Integrated XFEM-CE analysis of delamination migration in multi-directional composite laminates. Composites Part A: Applied Science and Manufacturing 90:161–173, DOI https://doi.org/10.1016/j.compositesa.2016.07.007
39. Makeev A, Seon G, Nikishkov Y, D N, P M, Robeson ME (2019) Analysis methods for improving confidence in material qualification for laminated composites. Journal of the American Helicopter Society 64(1):1–13, DOI https://doi.org/10.4050/JAHS.64.012006
40. Masaki H, Tadashi A, Mototsugu T, Taiji A, Shojiro O, Yoshihiro E (2006) Modes i and ii interlaminar fracture toughness and fatigue delamination of cf/epoxy laminates with self-same epoxy interleaf. International Journal of Fatigue 28(10):1154–1165, DOI 10.1016/j.ijfatigue.2006.02.004, the Third International Conference on Fatigue of Composites
41. Czabaj MW, Ratcliffe JG (2013) Comparison of intralaminar and interlaminar mode I fracture toughnesses of a unidirectional IM7/8552 carbon/epoxy composite. Composites Science and Technology

89:15–23, DOI 10.1016/j.compscitech.2013.09.008
42. Jirásek M, Zimmermann T (1998) Rotating Crack Model with Transition to Scalar Damage. Journal of Engineering Mechanics 124(3):277–284, DOI 10.1061/(ASCE)0733-9399(1998)124:3(277)
43. Rots JG (1988) Computational modeling of concrete fracture. PhD thesis
44. Pernice MF, De Carvalho NV, Ratcliffe JG, Hallett SR (2015) Experimental study on delamination migration in composite laminates. Composites Part A: Applied Science and Manufacturing 73:20–34, DOI https://doi.org/10.1016/j.compositesa.2015.02.018